Chapter 2
Estimation of Fault Rupture Extent Using Near-Source Records for Earthquake Early Warning

M. Yamada

Abstract This chapter presents a methodology to estimate fault rupture extent in real time for the earthquake early warning. This approach identifies the fault rupture geometry by classifying stations into near source and far source. Suppose there is a sufficiently dense seismic network, the distribution of the near-source station can be used for identifying the fault geometry. In this chapter, we improved a discriminant function to classify seismic records into near-source or far-source records proposed in the previous work. We added the earthquake dataset obtained after 2007, and updated the discriminant function. Furthermore, we integrate the information on each station and proposed a methodology to display the fault rupture surface from the distribution of near-source stations. The probability that a station is near-source obtained from this optimal discriminant function shows the extent of the near-source area reasonably well, suggesting that the approach provides a good indicator of near-source and far-source stations for real-time analyses. After applying interpolation, we successfully displayed the fault rupture surface from the distribution of near-source stations.

2.1 Introduction

Earthquake Early Warning provided for public people in Japan by Japan Meteorological Agency (JMA) is one of the most advanced real-time warning systems in the world. The earthquake early warning system, which provides information about strong shaking within seconds of a quake, has been in place since October 2007 and has provided more than 10 warnings of strong earthquakes—by cellular phone, television, radio and local-community speaker system.

On March 11 2011, the earthquake early warning system detected the earthquake off the Pacific coast of Tohoku (hereafter the 2011 Tohoku earthquake), and about

M. Yamada (✉)
Disaster Prevention Research Institute, Kyoto University, Kyoto, Japan
e-mail: masumi@eqh.dpri.kyoto-u.ac.jp

F. Wenzel and J. Zschau (eds.), *Early Warning for Geological Disasters*,
Advanced Technologies in Earth Sciences, DOI: 10.1007/978-3-642-12233-0_2,

8 s after the first P-wave detection at the closest seismic station, issued a warning to the public in the Tohoku region close to the epicenter (Japan 2011). However, the overall performance of the system was not satisfactory, mainly because of the complex character and relatively small amplitude of the beginning of the rupture. The system underestimated ground motion because current JMA system assumes a point source, and does not consider fault finiteness. However, the rupture of the 2011 Tohoku earthquake extended as far as 500 km away, so the large population in the greater Tokyo region, where many areas experienced strong and damaging shaking, received no warning. That said, updates did improve as more information became available (Sagiya et al. 2011).

For the accurate ground motion estimation, it is important to estimate fault rupture extent in real time. Izutani and Hirasawa (2003) presented a method to determine fault parameters of large shallow earthquake from azimuthal dependence of strong motion duration due to directivity. Yamada et al. (2007) proposed a methodology to identify the fault rupture geometry by classifying stations into near source and far source. Recently, the estimation of rupture dimension attracts research attention and several new approaches were proposed (Horiuchi and Horiuchi 2011; Yamada and Heaton 2008; Yamamoto et al. 2008).

In order to estimate the fault rupture extent in real time, we use the same approach with Yamada et al. (2007). Suppose there is a sufficiently dense seismic network, the distribution of the near-source station can be used for identifying the fault geometry. Yamada et al. (2007) proposed a discriminant function to classify seismic records into near-source or far-source records. In this chapter, we added the earthquake dataset obtained after the work of Yamada et al. (2007), and updated the discriminant function. Furthermore, we integrate the information on each station and proposed a methodology to display the fault rupture surface from the distribution of near-source stations.

2.2 Data

We used strong-motion records of seventeen shallow crustal earthquakes with magnitude greater than 6.0 and containing records of near-source stations. The selected earthquakes are shown in Table 2.1. Here, we define a near-source station as a station whose fault distance is less than 10 km. In this chapter, the definition of the fault distance is the shortest distance between the station and the surface projection of the fault rupture surface (Joyner-Boore distance) (Joyner and Boore 1981). 1319 three-component strong-motion data are used for the classification analysis, and 11 % (142 records) are from near-source stations. The source of new records, not included in Yamada et al. (2007), were the K-net, KiK-net, and JMA strong motion network. The classification as near source or far source in the dataset is based on rupture area models used for waveform inversions. Fault models used for classifying stations are also shown in Table 2.1. If the Joyner-Boore distance is less than 10 km, we define the station as a near source. This dataset is used as a training dataset of the classification problem.

Table 2.1 List of the earthquake dataset used for the classification analysis

Earthquake	Year	Date	Mw	NS	FS	Total	ARV	Reference
Imperial Valley	1979	10/15	6.5	14	20	34		Hartzell and Heaton (1983)
Loma Prieta	1989	10/17	6.9	8	38	46		Wald et al. (1991)
Landers	1992	6/28	7.3	1	35	36		Wald and Heaton (1994)
Northridge	1994	1/17	6.6	17	133	150		Wald et al. (1996)
Kobe	1995	1/17	6.9	4	14	18		Wald (1996)
Izmit	1999	8/17	7.6	4	10	14		Sekiguchi and Iwata (2002)
Chi-Chi	1999	9/20	7.6	42	169	211		Ji et al. (2003)
Western Tottori*	2000	10/6	6.7	5	96	101	X	Semmane et al. (2005)
Denali	2002	11/3	7.8	1	3	4		Tsuboi et al. (2003)
Niigataken-Chuetsu	2004	10/23	6.6	13	95	108	X	Honda et al. (2005)
Noto-Hanto*	2007	3/25	6.7	3	46	49	X	Shiba (2008)
Niigataken-Chuetsuoki*	2007	7/16	6.6	7	76	83	X	Aoi et al. (2008)
Wenchuan*	2008	5/12	7.9	6	34	40		Koketsu et al. (2008)
Iwate-Miyagi*	2008	6/14	6.9	6	115	121	X	Suzuki et al. (2010)
Surugawan*	2009	8/11	*6.4	3	121	124	X	Aoi et al. (2010)
Northern Nagano*	2011	3/12	6.3	4	95	99	X	Hata et al. (2012)
Fukushima-Hamadori*	2011	4/11	6.7	4	77	81	X	Somei et al. (2011)
Total				142	1177	1319		

Asterisks after the earthquake name indicate that the data was not used in Yamada et al. (2007) and new in this article. Moment magnitude (Mw) is cited from the Harvard Centroid Moment Tensor solution and USGS for the Surugawan earthquake. The numbers of near-source (NS) and far-source (FS) data for each earthquake are also shown. Availability of site amplification factors is shown in the column of ARV. The fault models in the reference are used as selection criteria to classify near-source and far-source stations

2.2.1 Data Processing

We processed the accelerograms obtained from the seventeen earthquakes according to the following method. A bias is removed from the accelerograms by subtracting the pre-event mean. The peak amplitudes of the horizontal components are calculated by the square root of the sum of squared maxima of north-south and east-west components. The peak amplitude of the up-down component is used directly for the peak vertical component. The following processes are completed for all the data.

- Jerk: The three-component accelerograms are differentiated in the time domain, using a simple finite-difference approximation. The peak value of each component is selected.
- Acceleration: Original accelerograms are used to select the peak value.
- Velocity: The acceleration records are integrated once in the time domain and are high-pass filtered using a fourth-order Butterworth filter with a corner frequency of 0.075 Hz.
- Displacement: The filtered velocity records are integrated once in the time domain and used as a displacement record.

The peak features used for the classification analysis are these four measurements and vertical and horizontal components in each measurement. Several combinations of these eight features are used to find the best performance of the classification.

2.2.2 Data Distribution

We compute the base 10 log of the ground motion amplitudes and find the means and standard deviations for the near-source and far-source records. Figure 2.1 shows the histograms and Gaussian densities given by the sample means and standard deviations of ground motion measures for the near-source and far-source records. The Gaussian densities are good approximations of the histograms of the log of the ground motion data. Figure 2.1 also shows that the distance between means for the near-source and far-source datasets is larger in high-frequency than low-frequency motions. Therefore, we expect that the high-frequency motion is a good measure to classify near-source and far-source records.

High-frequency near-source ground motions have long been researched by engineers and seismologists. High-frequency ground motions depend weakly on magnitude in the near-source (Hanks and Johnson 1976; Hanks and McGuire 1981; Joyner and Boore 1981). This helps to analyze ground motions with a wide range of magnitude. On the other hand, low-frequency motion has a strong correlation with magnitude and its amplitude increases as the magnitude becomes large. High-frequency ground motion decays in amplitude more rapidly with distance than low-frequency motion (Hanks and McGuire 1981). Therefore, high-frequency motion (e.g. acceleration, jerk) has high correlations with the fault distance (Campbell 1981) and is a good proxy to classify near-source and far-source records.

2.2.3 Soil Amplification Factors

In order to consider amplification of the subsurface soil, site amplification factors (ARV) are computed for the strong motion data recorded in Japan. ARV stands for amplitude ratio of PGV at the ground surface relative to engineering bedrock with average S-wave velocity 700 m/s. K-NET and KiK-net provide velocity structures obtained from logging data, so the average S-wave velocity (m/s) from surface to 30 m depth (Vs30) can be computed from the velocity structures. The site amplification factor between surface and engineering bedrock (Vs $=$ 600 m/s) has a following relationship with Vs30 (Midorikawa et al. 1992).

$$\mathrm{ARV} = 10^{(1.83-0.66(\log_{10}(\mathrm{Vs30})))} \tag{2.1}$$

For stations without logging data, ARV is computed by the method proposed by Matsuoka et al. (2005). This approach uses microtopography to estimate ARV.

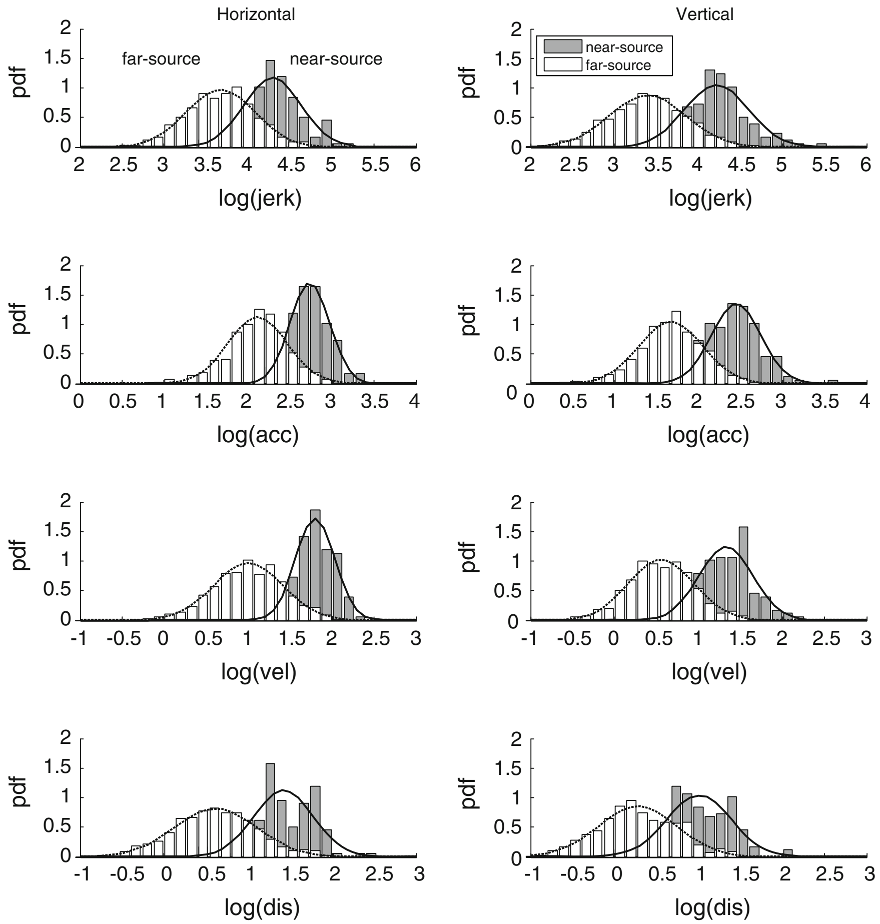

Fig. 2.1 Histograms and Gaussian densities based on the sample means and standard deviations of the log of ground motions for the near-source and far-source records. These are distributions for jerk, acceleration, velocity, and displacement from the *top*

Because the ARV is the amplification from the engineering bedrock to the surface, the velocity records at the engineering bedrock are estimated as ground velocity records divided by ARV. The ARV-corrected velocity records are used in Sect. 2.4.3.

2.3 Method

In order to estimate the fault rupture extent in real time, we use the same approach with Yamada et al. (2007). Suppose there is a sufficiently dense seismic network, the distribution of the near-source station can be used for identifying the fault geometry.

Adding the earthquake dataset obtained after the work of Yamada et al. (2007), we update the discriminant function to classify seismic records into near-source or far-source records. To estimate the fault rupture extent in real time, we take the following three steps:

(1) Prepare a training dataset. Collect strong motion data from earthquake strong motion archives and discover a discriminant function which provides the best performance in terms of near-source/far-source classification.
(2) Allocate new observations when they are obtained to one of the two groups based on the discriminant function.
(3) Integrate this near-source information and display the 2D fault rupture surface by interpolation technique.

We developed a new approach to estimate 2D fault rupture dimension from the discriminant function (see Sect. 2.3.2). We also examined the effect of dataset, discriminant boundary, and the correction of site amplification factor, which are not included in the previous work.

2.3.1 Near-Source and Far-Source Discriminant Function

We assume the discriminant function to classify records into near source and far source is expressed as a linear combination of the log of ground-motion amplitudes:

$$f(X_i|\theta) = c_1 x_{i1} + c_2 x_{i2} + \ldots + c_m x_{im} + d = \sum_{k=1}^{m} c_k x_{ik} + d \tag{2.2}$$

where x_{ik} is the kth feature parameter of the ground motion at the ith station, m is the number of feature parameters, $X_i = [x_{i1}, x_{i2}, \ldots, x_{im}] =$ [log$_{10}$(component 1); log$_{10}$(component 2); …; log$_{10}$(component m)], $c_1, \ldots, c_m$ is the regression coefficients, d is the decision boundary constant, and $\theta = [c_1, c_2, \ldots, c_m, d]^{\mathrm{T}}$. We may use m components out of the eight ground-motion components. The coefficients $c_1, \ldots, c_m$ and d are determined from the training dataset by Bayesian analysis. This discriminant function is used to allocate new observations to one of the near-source or far-source groups, where $f(X_i|\theta) = 0$ is the boundary between the two groups in the feature parameter space. The station with observation X_i is classified as near source if $f(X_i|\theta)$ is positive. If $f(X_i|\theta)$ is negative, the station is classified as a far-source station.

We define the predictive probability that the ith station is near source by applying the logistic sigmoid function;

$$P(X_i, \theta) = 1/(1 + e^{-f(X_i|\theta)}) \tag{2.3}$$

As $f(X_i|\theta)$ becomes larger, the station is more likely to be near source, and the probability that the station is near-source becomes closer to one. The predictive probability that the station is far-source is then $1 - P(X_i, \theta)$.

The probability density function (pdf) of parameter θ conditioned on data *Dn* and model class *M* can be expressed using Bayes's theorem (Yamada et al. 2007):

$$P(\theta|D_n, M) \propto 1/(\sqrt{2\pi}\sigma)^{m+1} \exp(-1/(2\sigma^2)\theta^T\theta \times \prod_{i=1}^{n} 1/(1 + e^{-f(X_i|\theta)}) \quad (2.4)$$

where σ is a standard deviation of the prior of each model parameter. Here, we select the prior of each model parameter to be a Gaussian PDF with zero mean and standard deviation $\sigma = 100$. We need to find the optimal parameter θ that maximizes this posterior pdf. Note that the model class *M* defines the combination of ground motion measures. This multidimensional optimization problem is solved by a numerical optimization algorithm provided by Matlab (Yamada et al. 2007).

Yamada et al. (2007) performed Bayesian model class selection and found the best combination of ground motion measures to provide the best performance of classification is the vertical acceleration and horizontal velocity. We performed this analysis with the new dataset, and the same combination was selected. Therefore, we use the following equation as a discriminant function.

$$f(X_i|\theta) = c_1 \log_{10} Za_i + c_2 \log_{10} Hv_i + d \quad (2.5)$$

where Za_i is the vertical acceleration and Hv_i is the horizontal velocity at the station i.

2.3.2 Estimating 2D Fault Rupture Dimension

The rupture estimation approach proposed in the previous section depends on the station density, and denser station distribution can provide more accurate estimation. The predictive probability that a station is near-source is assigned to a location of the station, so it would be useful if we can transfer this information at a point to information on the surface. Here, we apply an interpolation and try to obtain the fault rupture surface from probability at each station. The probability *P(Y)* that a site *Y* is near-source is expressed as a sum of weighted probability of station *i*:

$$P(Y) = \sum_{i=1}^{n} [2P(X_i, \theta) - 1]w(R_i), \quad (2.6)$$

where n is the number of stations, R_i is Joyner-Boore distance between station i and site Y, $w(R_i)$ is a weighting as a function of distance and density parameter ρ.

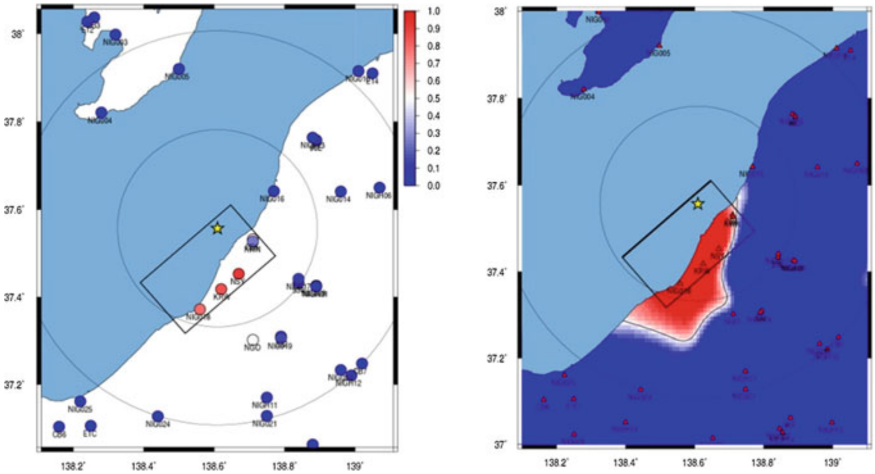

Fig. 2.2 The probability that the station is near source at each station (*left*) and estimated fault rupture surface by interpolation technique (*right*). The *red color* has higher probability that the station is located at near source, and the *blue color* has higher probability that the station is located at far source. The fault projections are shown in the *solid lines*. The *star symbol* denotes the epicenter of the earthquake

$$w(R_i) = \begin{cases} 1 & if \;\; R_i < 10[km] \\ 0.5(\cos\;[180(R_i - 10)/(\rho - 10)] + 1) & if \;\; 10 \le R_i < \rho[km] \\ 0 & if \;\; R_i \ge \rho[km] \end{cases} \quad (2.7)$$

The density parameter ρ is determined based on the station spacing. The interpolation efficiency can be maximized if you use average station spacing for ρ. If ρ is too large against the station spacing, the probability at a site is affected by a station far away. If ρ is too small, there are many sites who cannot obtain the probability since all $w(R_i)$ becomes zero. As for Japanese seismic network, the average station spacing is about 20 km, so $\rho = 20$ is used as a proper density parameter. We assumed the location of an epicenter is given and used the epicenter as a single 'near-source' station with probability $P(X_i, \theta) = 1$. The performance is shown in Fig. 2.2.

The rupture surface can be approximately estimated even the station density is not dense enough by applying this interpolation technique. For example, the station spacing of 2008 Wenchuan earthquake is about 50 km. However, the fault rupture extends as far as a couple of hundred km, the rupture dimension can be estimated by setting $\rho = 50$. Ideally, the station spacing for accurate fault rupture estimation is 10–20 km.

2.4 Results

We obtained a discriminant function classifying near-source and far-source stations that maximizes the posterior pdf. We used two different dataset: All dataset (Japanese + outside of Japan) and Japanese dataset. We also examined the effect of fault distance considering dip angle in the Sect. 2.4.2, and effect of site amplification factor (ARV) in the Sect. 2.4.3.

2.4.1 Classification Function with All Datasets

Table 2.2 shows the optimal parameters for the classification function obtained from Yamada et al. (2007) and all dataset in this chapter. Evidence is an index to select the optimal model class if the same dataset was used (Yamada et al. 2007). Note that the evidence is log-scaled, and the larger value of the evidence indicates a better fit to the dataset. The evidence of the previous work shows the smaller value, but we cannot compare the evidence of the different datasets. The ratios of the parameters are very similar, meaning both discriminate functions provide very similar result to classify near-source and far-source stations. The optimal discriminant function with all dataset is expressed as:

$$f(X_i|\theta) = 4.40 \log_{10} Za_i + 5.17 \log_{10} Hv_i - 19.12. \tag{2.8}$$

where Za_i is the vertical acceleration and Hv_i is the horizontal velocity at the station i.

The classification performance of the discriminant function obtained from all dataset is shown in Fig. 2.3 and confusion matrix is shown in Table 2.3. Circle symbols show the near-source records and cross symbols show the far-source records. Suppose the 50 % of the probability is a boundary of near source and far source, black symbols are correctly classified, and red symbols are incorrectly classified. This figure shows most of the misclassified records are located at the boundary of the near source and far source (about 10 km of the fault). We found that the near-source data with very low probability of near-source were located at the edge of the fault, which indicates that the fault models used here are those from the source inversion and not necessarily the best indicator of near-source and far-source stations.

Table 2.2 The optimal parameters for the discriminant functions based on the all dataset in this chapter and dataset of Yamada et al. (2007)

	c_1	c_2	d	Evidence
Yamada et al. (2007)	6.05	7.89	−27.09	−96
All dataset in this chapter	4.40	5.17	−19.12	−179

The values for the evidence of each model class are log-scaled

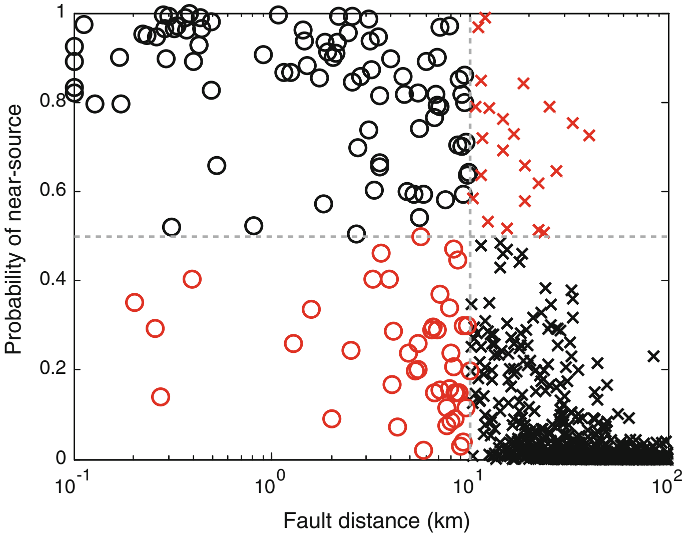

Fig. 2.3 The classification performance of the discriminant function from all dataset in this chapter. *Circle symbols* show the near-source records and *cross symbols* show the far-source records. Suppose the 50 % of the probability is a boundary of near source and far source, *black symbols* are correctly classified, and *red symbols* are incorrectly classified

We performed the leave-one-out cross validation to check the robustness of the discriminant function. The idea of this method is to predict the probability of a station from the discriminant function constructed from the dataset from which that station is excluded. This process is repeated for all 1319 data, and the accuracy of prediction is computed. The percentage of misclassified data is only 5 % (68/1319). Therefore, we conclude that the discriminant function is stable enough for a new dataset which is not included in the training dataset (Figs. 2.4 and 2.5).

2.4.2 Effect of Dip Angle of the Fault

As a boundary of near-source and far-source, we use the Joyner-Boore distance. In this section, we consider dip angle of the fault and use shortest distance between a station and the fault rupture surface (i.e. fault distance). We compared the classification performance with the boundary of 10 km of these distance definitions. Table 2.4

Table 2.3 Confusion matrix for near-source versus far-source classification by the discriminant function from all dataset in this chapter

Dataset	NS	FS
Classified as NS	88 (66 %)	23 (2 %)
Classified as FS	45 (34 %)	1163 (98 %)

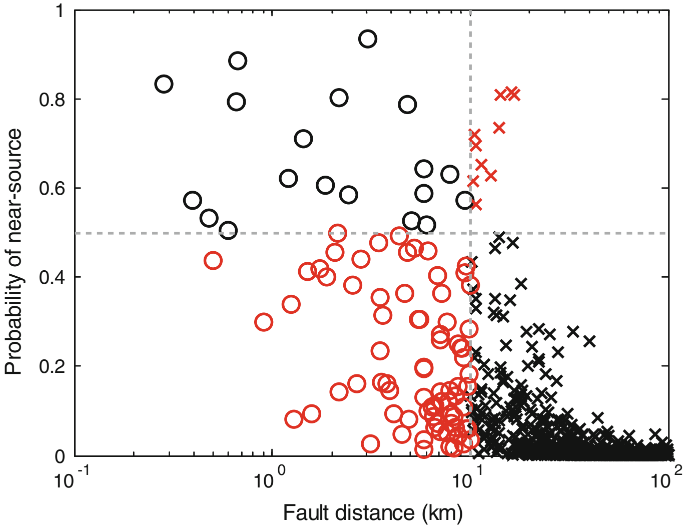

Fig. 2.4 The classification performance of the discriminant function from all dataset with rupture distance. *Circle symbols* show the near-source records and *cross symbols* show the far-source records. Suppose the 50 % of the probability is a boundary of near source and far source, *black symbols* are correctly classified, and *red symbols* are incorrectly classified

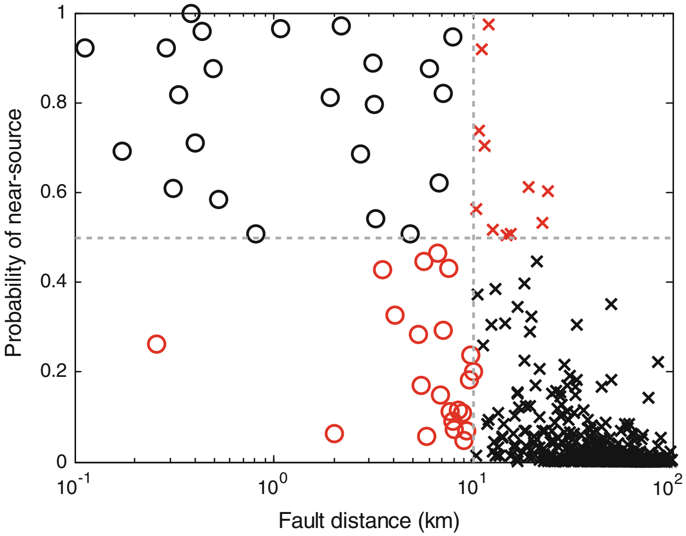

Fig. 2.5 The classification performance of the discriminant function from Japanese dataset with ARV correction. *Circle symbols* show the near-source records and *cross symbols* show the far-source records. Suppose the 50 % of the probability is a boundary of near source and far source, *black symbols* are correctly classified, and *red symbols* are incorrectly classified

Table 2.4 The optimal parameters for the discriminant functions based on the all dataset with Joyner-Boore distance and rupture distance as a boundary of near source and far source

	c_1	c_2	d	Evidence
Joyner-Boore distance	4.40	5.17	−19.12	−179
Rupture distance	2.18	4.61	−13.89	−196

The values for the evidence of each model class are log-scaled

shows the optimal parameters for the discriminant function and evidence of each model. The model with Joyner-Boore distance is better than the model with rupture distance. This implies that the amplitudes of ground motion have better correlation with Joyner-Boore distance. Although Joyner-Boore distance and rupture distance are exactly the same for the strike-slip fault mechanism, the Joyner-Boore distance is shorter than rupture distance for the thrust fault event. If the station is located on the hanging-wall, the amplitude tends to be large. In such a case, Joyner-Boore distance is a constant but rupture distance becomes longer depending on the dip angle. Therefore, to classify near-source and far-source records, Joyner-Boore distance shows the better classification performance and that means it is difficult to estimate the dip angle of the fault from this approach.

The evidence of the ARV corrected discriminant function is slightly smaller than the discriminant function with no ARV correction. However, the ARV corrected discriminant function can provide smaller variance on the probability if two stations are close each other. Therefore, if the ARV at a site is available, it is better to use Eq. 2.9.

2.4.3 Effect of Soil Amplification

Ground motions are amplified by the subsurface soil, so the amplitude depends on the subsurface soil structure. Especially velocity records are strongly affected by the site amplification factor (ARV) between surface and engineering bedrock (Midorikawa et al. 1992). We used Japanese dataset whose ARV at the station is available and compared the results of corrected velocity records by ARV with the results of uncorrected velocity records. Although acceleration records are also affected by the subsurface soil structure, the amplification characteristics are more complicated and difficult to evaluate (Si and Midorikawa 2000). Therefore, we consider only the effect of ARV on velocity records (Tables 2.5, 2.6 and 2.7).

The optimal discriminant function with ARV correction is:

$$f(X_i|\theta) = 4.35 \log_{10} Za_i + 2.82 \log_{10}(Hv_i/ARV_i) - 14.89. \tag{2.9}$$

where ARV_i is site amplification factor at the station i.

Table 2.5 Confusion matrix for near-source versus far-source classification by the discriminant function from all dataset with rupture distance

Dataset	NS	FS
Classified as NS	19 (19 %)	10 (1 %)
Classified as FS	79 (81 %)	1211 (99 %)

Table 2.6 The optimal parameters for the discriminant functions based on the Japanese dataset with and without ARV correction

	c_1	c_2	d	Evidence
No ARV	3.98	3.47	−15.50	−89
ARV corrected	4.35	2.82	−14.89	−93

The values for the evidence of each model class are log-scaled

Table 2.7 Confusion matrix for near-source versus far-source classification by the discriminant function from Japanese dataset with ARV correction

Dataset	NS	FS
Classified as NS	23 (51 %)	22 (2 %)
Classified as FS	11 (49 %)	710 (98 %)

2.4.4 Estimated Rupture Dimension

We apply the optimal discriminant function (in Eq. 2.9) to all the stations in the Japanese dataset and estimated the fault rupture extent by applying the interpolation. Figure 2.6 shows the results of estimation. The regions with a high probability of being in the near-source are consistent with the area within 10 km from fault geometry in the most cases. As mentioned before, the fault models that are used here are those from the source inversion, and they are not necessarily the best indicator of near-source and far-source stations.

This approach also works for dataset whose ARV is not available. We apply the optimal discriminant function (in Eq. 2.9) to dataset whose site condition is unknown, and estimated the fault rupture extent by applying the smoothing filter. Figure 2.7 shows the results of estimation. If the number of near-source station is too small against the size of earthquake, the result is very poor. The 1992 Landers, 1999 Izmit, and 2002 Denali earthquakes show poor estimation of the fault rupture extent. However, the number of near-source station is greater than five, the estimated near-source region is in general consistent with the fault rupture surface. 1999 Chi-Chi and 2008 Wenchuan earthquakes have larger magnitude than Japanese earthquakes shown in Fig. 2.6, but the results shows reasonably good performance to estimate fault rupture dimension.

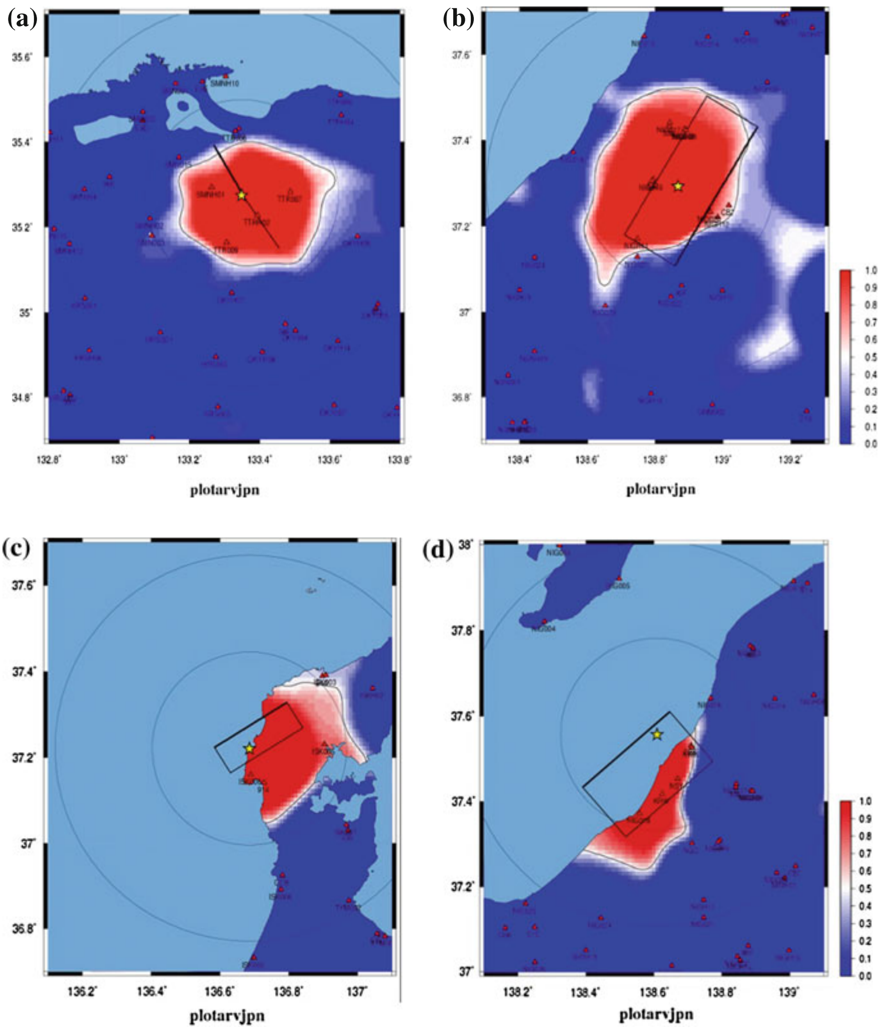

Fig. 2.6 Estimated fault rupture surface for Japanese earthquakes. The *red color* has higher probability that the region is located at near source, and the *blue color* has higher probability that the region is located at far source. The symbols for the fault and epicenter are the same as in Fig. 2.2. **a** 2000 Western Tottori **b** 2004 Niigataken-Chuetsu **c** 2007 Noto-Hanto **d** 2007 Niigataken-Chuetsuoki **e** 2008 Iwate-Miyagi **f** 2009 Surugawan **g** 2011 Northern Nagano **h** 2011 Fukushima-Hamadori

2.5 Conclusion

In this chapter, extending the concept of Yamada et al., we proposed a new discriminant function to classify seismic records into near-source or far-source records. Furthermore, we integrate the information on each station and proposed a methodol-

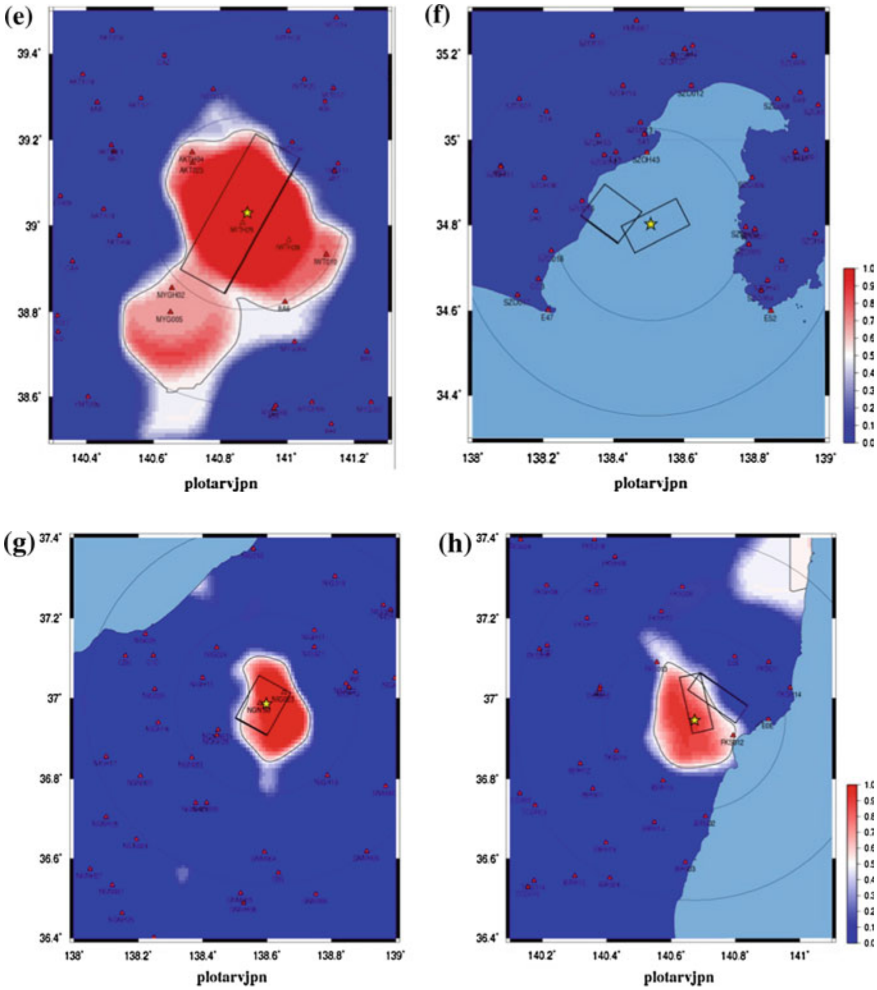

Fig. 2.6 Continued

ogy to display the fault rupture surface from the distribution of near-source stations. We constructed a new dataset of the latest large earthquakes and analyzed them to find a linear function that best discriminates near-source and far-source records. The best discriminant function is:

$$\begin{array}{ll} f(X_i|\theta) = 4.30\log_{10} Za_i + 5.09\log_{10} Hv_i - 18.77, & \text{if ARV is unknown} \\ f(X_i|\theta) = 4.26\log_{10} Za_i + 2.63\log_{10}(Hv_i/ARV_i) - 14.50, & \text{if ARV is available} \\ P(X_i,\theta) = 1/(1+e^{-f(X_i|\theta)}) & \end{array} \tag{2.10}$$

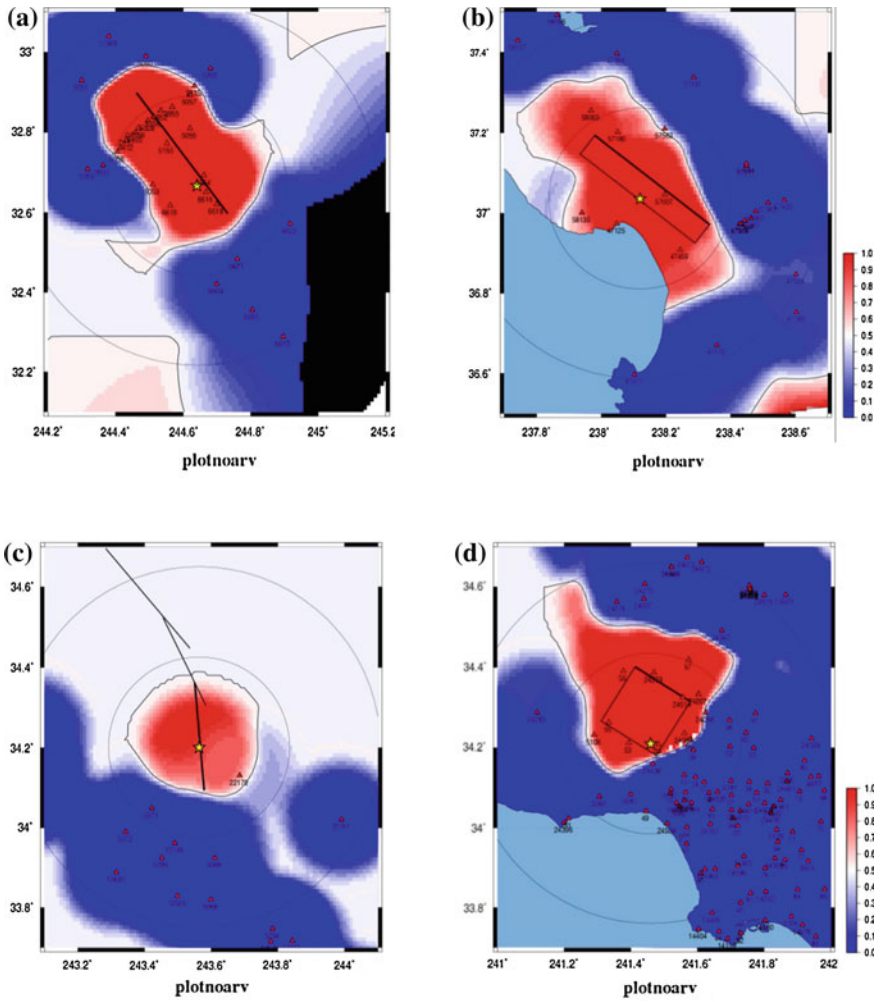

Fig. 2.7 Estimated fault rupture surface for earthquakes whose site condition is unknown. The *red color* has higher probability that the region is located at near source, and the *blue color* has higher probability that the region is located at far source. The symbols for the fault and epicenter are the same as in Fig. 2.2. **a** 1979 Imperial Valley **b** 1989 Landers **c** 1992 Landers **d** 1994 Northridge **e** 1995 Kobe **f** 1999 Izmit **g** 2002 Denali **h** 1999 Chi-Chi **i** 2008 Wenchuan

where Za_i and Hv_i denote the peak values of the vertical acceleration and horizontal velocity, respectively, and $P(X_i, \theta)$ is the probability that a station is near-source. This function indicates that the amplitude of high-frequency components is effective in classifying near-source and far-source stations.

The probability that a station is near-source obtained from this optimal discriminant function for all the earthquakes shows the extent of the near-source area quite

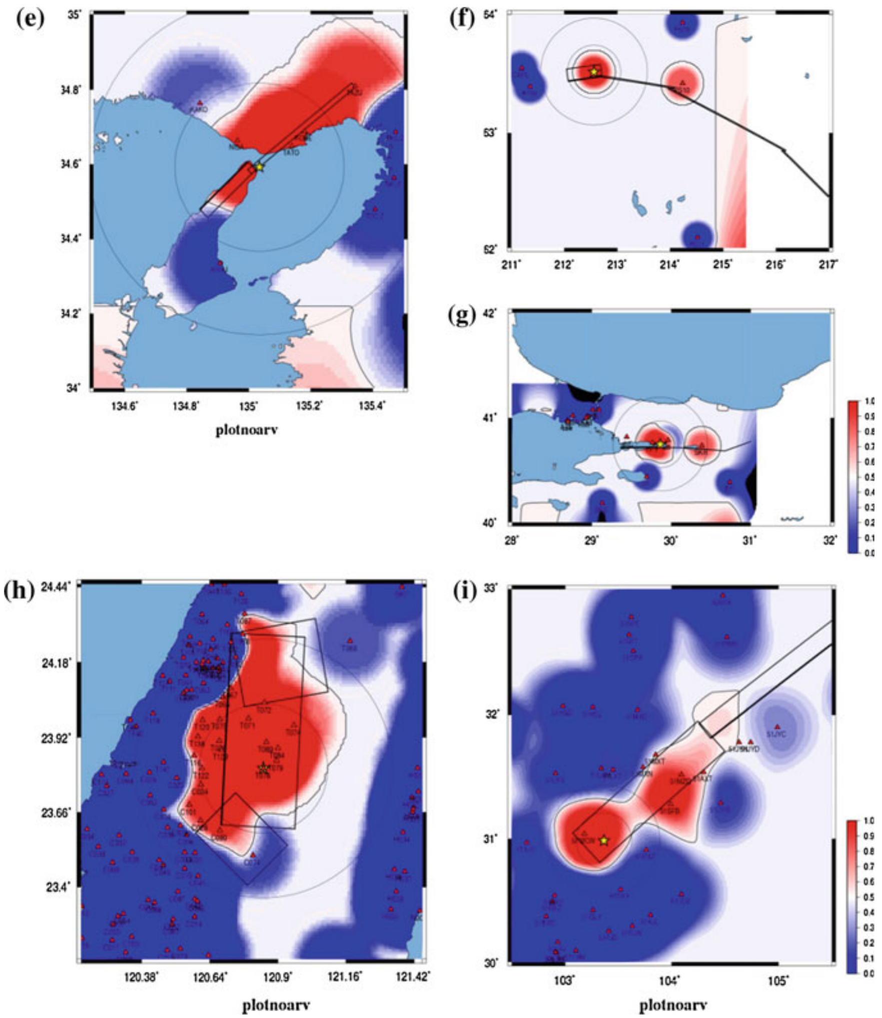

Fig. 2.7 continued

well, suggesting that the approach provides a good indicator of near-source and far-source stations for real-time analyses. After applying interpolation, we successfully displayed the fault rupture surface from the distribution of near-source stations. The regions with a high probability of being in the near-source are consistent with the area within 10 km from fault geometry in the most cases. Note that this function is constructed by the training dataset with magnitude greater than 6.2, so it only works for large earthquakes.

Acknowledgments The authors acknowledge the National Research Institute for Earth Science and Disaster Prevention (NIED) and Japan Meteorological Agency (JMA) for the use of the seismic data. Some of the figures are generated by Generic Mapping Tools (Wessel and Smith 1991).

References

Aoi S, Enescu B, Suzuki W, Asano Y, Obara K, Kunugi T, Shiomi K (2010) Stress transfer in the Tokai subduction zone from the 2009 Suruga Bay earthquake in Japan. Nat Geosci 3(7):496–500

Aoi S, Sekiguchi H, Morikawa N, Kunugi T (2008) Source process of the 2007 Niigata-ken Chuetsu-oki earthquake derived from near-fault strong motion data. Earth Planets and Space (EPS) 60(11):1131

Campbell KW (1981) Near-source attenuation of peak horizontal acceleration. Bull Seismol Soc Am 71(6):2039–2070

Hanks TC, Johnson DA (1976) Geophysical assessment of peak accelerations. Bull Seismol Soc Am 66(3):959–968

Hanks TC, McGuire RK (1981) The character of high-frequency strong ground motion. Bull Seismol Soc Am 71(6):2071–2095

Hartzell SH, Heaton TH (1983) Inversion of strong ground motion and teleseismic waveform data for the fault rupture history of the 1979 Imperial Valley, California, earthquake. Bull Seismol Soc Am 73(6A):1553–1583

Hata Y, Murata A, Nozu A, Miyajima M (2012) Ground motion evaluation at Yokokura village for the 2011 Nagano—Niigata border earthquake based on the site effects substitution method. J Jpn Assoc Earthq Eng

Honda R, Aoi S, Morikawa N, Sekiguchi H, Kunugi T, Fujiwara H (2005) Ground motion and rupture process of the 2004 Mid Niigata prefecture earthquake obtained from strong motion data of K-NET and KiK-net. Earth Planets and Space 57(6):527–532

Horiuchi S, Horiuchi Y (2011) Real-time location of fault area distribution for the Tsunami warning and shaking intensity estimation of a massive scale earthquake. Seismological Society of Japan, Shizuoka

Izutani Y, Hirasawa T (1987) Use of strong motion duration for rapid evaluation of fault parameters. J Phys Earth 35(2):171–190

JapanMeteorologicalAgency Earthquake early warning for the 2011 off the Pacific coast of Tohoku Earthquake (2011) [cited 2012 June 27]. http://www.seisvol.kishou.go.jp/eq/EEW/kaisetsu/joho/20110311144640/content/contentout.html

Ji C, Helmberger DV, Wald DJ, Ma KF (2003) Slip history and dynamic implications of the 1999 Chi-Chi, Taiwan, earthquake. J Geophys Res 108(B9):2412

Joyner WB, Boore DM (1981) Peak horizontal acceleration and velocity from strong-motion records including records from the 1979 Imperial Valley, California, earthquake. Bull Seismol Soc Am 71(6):2011–2038

Koketsu K, Yokota Y, Ghasemi H, Hikima K, Miyake H, Wang Z (2008) Source process and ground motions of the 2008 Wenchuan Earthquake, China, grant-in-aid for special purposes of 2008, MEXT, No. 20900002

Matsuoka M, Wakamatsu K, Fujimoto K, Midorikawa S (2005) Nationwide site amplification zoning using GIS-based Japan engineering geomorphologic classification map. In: 9th International conference on structural safety and reliability, Rome

Midorikawa S, Matsuoka M, Sakugawa K (1992) Evaluation of site effects on peak ground acceleration and velocity observed during the 1987 Chiba-ken-toho-oki earthquake. J Struct Constr Eng, AIJ 442:71–78

Sagiya T, Kanamori H, Yagi Y, Yamada Y, Mori J (2011) Rebuilding seismology. Nature 473: 146–148

Sekiguchi H, Iwata T (2002) Rupture process of the 1999 Kocaeli, Turkey, earthquake estimated from strong-motion waveforms. Bull Seismol Soc Am 92(1):300–311

Semmane F, Cotton F, Campillo M (2005) The 2000 Tottori earthquake: a shallow earthquake with no surface rupture and slip properties controlled by depth. J Geophys Res 110(B3):B03306

Shiba Y (2008) Rupture process during the 2007 Noto Hanto earthquake (MJMA 6.9) and strong-motion simulation in the source region. Earth Planets and Space (EPS), 60(10):1023–1028

Si H, Midorikawa S(2000) New attenuation relations for peak ground acceleration and velocity considering effects of fault type and site condition. In: 12th World conference on earthquake engineering

Somei K, Miyakoshi K, Irikura K (2011) Estimation of source model and strong motion simulation for the 2011 East Fukushima prefecture earthquake using the empirical Green's function method. Seismological Society of Japan, Shizuoka

Suzuki W, Aoi S, Sekiguchi H (2010) Rupture process of the 2008 Iwate-Miyagi Nairiku, Japan, earthquake derived from near-source strong-motion records. Bull Seismol Soc Am 100(1):256–266

Tsuboi S, Komatitsch D, Ji C, Tromp J (2003) Broadband modeling of the 2002 Denali fault earthquake on the earth simulator. Phys Earth Planet Inter 139(3–4):305–313

Wald DJ (1996) Slip history of the 1995 Kobe, Japan, earthquake determined from strong motion, teleseismic, and geodetic data. J Phys Earth 44(5):489–504

Wald DJ, Heaton TH (1994) Spatial and temporal distribution of slip for the 1992 Landers, California, earthquake. Bull Seismol Soc Am 84(3):668–691

Wald DJ, Heaton TH, Hudnut KW (1996) The slip history of the 1994 Northridge, California, earthquake determined from strong-motion, teleseismic, GPS, and leveling data. Bull Seismol Soc Am 86(1B):S49–S70

Wald DJ, Helmberger DV, Heaton TH (1991) Rupture model of the 1989 Loma Prieta earthquake from the inversion of strong-motion and broadband teleseismic data. Bull Seismol Soc Am 81(5):1540–1572

Wessel P, Smith WHF (1991) Free software helps map and display data. EOS 72(441):445–446

Yamada M, Heaton TH (2008) Real-time estimation of fault rupture extent using envelopes of acceleration. Bull Seismol Soc Am 98(2):607–619

Yamada M, Heaton TH, Beck J (2007) Real-time estimation of fault rupture extent using near-source versus far-source classification. Bull Seismol Soc Am 97(6):1890–1910

Yamamoto S, Horiuchi S, Nakamura H, Wu C, Irikura K, Fukushima Y (2008) Seismic intensity estimation taking into account fault finiteness for earthquake early warning. In: Japan Geoscience Union meeting, Chiba

http://www.springer.com/978-3-642-12232-3

Early Warning for Geological Disasters
Scientific Methods and Current Practice
Wenzel, F.; Zschau, J. (Eds.)
2014, XV, 379 p., Hardcover
ISBN: 978-3-642-12232-3